Design strong anomalous Hall effect via spin canting in antiferromagnetic nodal line materials

Congcong Le ☉,[1,2] Claudia Felser,[1] and Yan Sun[1,*]

[1]*Max Planck Institute for Chemical Physics of Solids, 01187 Dresden, Germany*
[2]*RIKEN Interdisciplinary Theoretical and Mathematical Sciences (iTHEMS), Wako, Saitama 351-0198, Japan*

The interplay between magnetism and the topological electronic structure provides a large freedom for designing strong anomalous Hall effect (AHE) materials. A nodal line from band inversion is a typical band structure for generating strong AHE. On the other band, in most collinear antiferromagnets (AFMs), the integral of the Berry curvatures on the Brillouin zone is forced to zero by the joint TO symmetry, where T and O are the time reversal and a space group operation, respectively. Even with inverted band structures, such AFM cannot have an AHE. Therefore, the AFM nodal line band structures constructed by spin degenerated bands do not receive much attention in AHE materials. In this work, we illustrate that such a band structure provides a promising starting point for generating strong local and net Berry curvature and, hence, strong intrinsic AHE. In specific AFM compounds of AMnBi$_2$ (A = Ca and Yb) with an inverted band structure, we observed a strong AHE induced by a weak spin canting from temperature or doping. The anomalous Hall conductivity continues to grow with the canting angle owing to the nodal line in the band structure. Since such spin canting can be adjusted experimentally via doping, it provides another effective strategy to generate and manipulate a strong AHE.

I. INTRODUCTION

In recent years, materials with a strong anomalous Hall effect (AHE) [1] have attracted extensive attention in the fields of materials science and condensed matter physics, which are connected to fundamental topological band structures and potential applications in electronic devices. Since the intrinsic AHE can be understood as the integral of the Berry curvature in the momentum space [2–4], band structures with strong Berry curvature are desired to obtain a strong AHE. Weyl points and nodal lines are two types of promising band structures, which can generate strong local Berry curvatures. Using this guiding principle, strong AHE materials with both large anomalous Hall conductivity (AHC) and anomalous angles were observed in the ferromagnetic Weyl semimetal Co$_3$Sn$_2$S$_2$ [5–7], nodal semimetals of layered ferromagnetic compound Fe$_3$GeTe$_2$ [8,9], and Heusler compound Co$_2$Mn(Ga/Al) [10–15] *et al.*

A crucial property of the Berry curvature is that it is odd under a time reversal operator [4]. Hence AHE can exist in a broken time-reversal system in the linear response region. Owing to the broken time reversal symmetry T, the ferromagnet can host a nonzero AHE. However, in the collinear antiferromagnets (AFM), despite the broken time reversal

operation T, there are two types of combined symmetries TO between the time reversal operation T and a unitary space group operation O, where O is a fractional translation or inversion symmetry. Then, the combined symmetry TO can also change the sign of the Berry curvature, resulting in the cancellation of the Berry curvature when integrated over the full Brillouin zone (BZ). Therefore, AHE can only exist in a few situations without the combined symmetries TO, such as noncollinear AFM in FeMn, NiS$_2$, cubic Mn$_3$(Ir/Pt) and hexagonal Mn$_3$(Ge/Sn) [16–22], and collinear AFM Ti$_2$MnAl and RuO$_2$ [23,24]. On the other hand, AMF with combined symmetries TO almost did not attract much attention in AHE materials, even with nodal-line-like special band structures. In addition, based on the effective model, high-temperature quantum AHE can be induced by canted antiferromagnetism [25]. Symmetry and effective model analysis in a two dimensional insulating system suggested the existence of the quantum anomalous Hall phase [25]. However, neither a strong or quantized anomalous Hall effect was observed in realistic materials. In this work, by using first principles, as we will show below, by spin canting, the nodal-line-like special band structures in the AFM materials with combined symmetries may generate strong AHE. In addition, the intrinsic contribution is mainly dependent on the electric structures, while the extrinsic effect depends on the details of scattering. Therefore, we mainly focus on the intrinsic contribution.

In this work, we propose an effective strategy for generating strong Berry curvature by spin-canting based on collinear AFM nodal line band structures with combined symmetries TO. Figures 1(a)–1(c) show the schematic of AHE in the spin canted AFM order with inverted band structure. At the canting angle $\theta = 0$, the bands are doubly degenerate owing to time
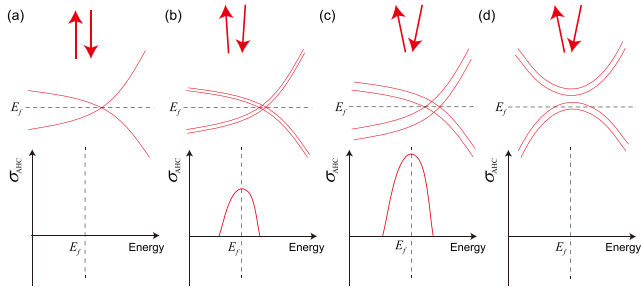
FIG. 1. Schematic of AHE in the spin canted AFM order with (a)–(c) and without (d) band inversion, where σ_{AHC} is the total value of AHC and E_f are the AHC and Fermi level, respectively. (a) Canting angle $\theta = 0$. (b) Small canting angle θ. (c) Large canting angle θ. (d) AHE in the spin canted AFM order without band inversion at a large canting angle θ.

reversal and inversion symmetries, and hence σ_{AHC} is zero, as shown in Fig. 1(a). When the canting angle θ is small, the two degenerate bands are split because of the broken time reversal symmetry, suggesting that σ_{AHC} should be nonzero, as shown in Fig. 1(b). Moreover, because the band inversion already exists in spin-degenerated bands, a canting can change the shape of the Berry curvature and AHC. When the canting angle θ becomes large, the two degenerate bands are split further and σ_{AHC} may become larger, as shown in Fig. 1(c). However, if the canted AFMs cannot host topological band structures, their AHEs are zero, as shown in Fig. 1(d). Based on the above schematic, we perform an *ab initio* analysis for AHE as the canting angle changes in the spin canting C-type AFM materials AMnBi$_2$ (A = Ca and Yb) [26–32], where the band inversion leads to a topological nodal ring without considering spin-orbit coupling (SOC). We find that the AHC continues to grow as the canting angle increases. Further, doping electrons can reduce the AHC while doping holes strengthen it.

II. METHOD AND SYMMETRY ANALYSIS

A. Method

Our calculations are performed using density functional theory (DFT) as implemented in the Vienna *ab initio* simulation package (VASP) code [33–35]. The Perdew-Burke-Ernzerhof (PBE) exchange-correlation functional and the projector-augmented-wave (PAW) approach are utilized. Throughout the work, the cutoff energy is set to be 550 eV to expand the wave functions into a plane-wave basis. The Brillouin zone is sampled in the k space within the Monkhorst-Pack scheme [36] and the k mesh used is $10 \times 10 \times 4$ on the basis of the equilibrium structure. In our calculations, a C-type AFM order along the c axis, a spin canting, and SOC are included. We use parameter "I-CONSTRAINED-M" to constrain the direction of the magnetic moments, and the size can be obtained by self-consistent calculation.

To calculate the AHC, we project the *ab initio* DFT Bloch wave function into highly symmetric atomic-orbital-like Wannier functions [37] with a diagonal position operator, as implemented in the Vienna *ab initio* simulation package (VASP) code [33–35]. To obtain precise Wannier functions, we
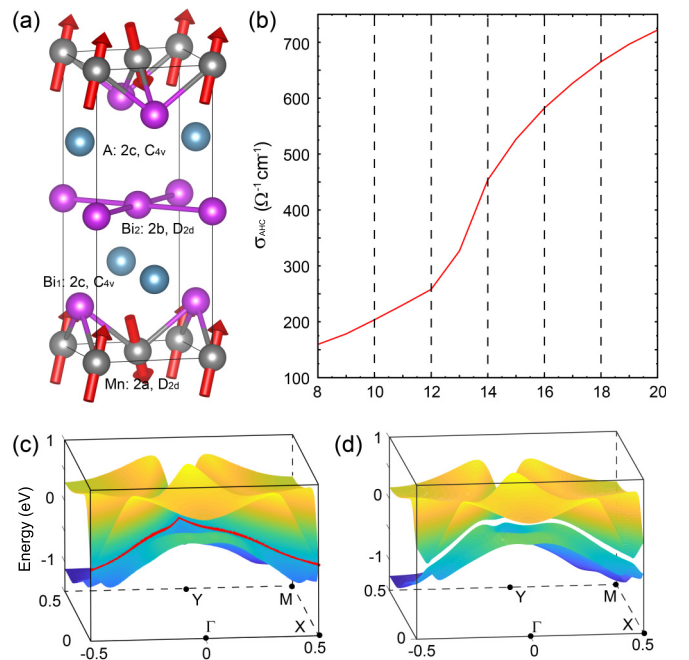

FIG. 2. (a) Crystal structure and C-type AFM order of AMnBi$_2$ with spin canting along the (1,1,0) direction. The Wyckoff positions and corresponding site symmetry groups are provided. (b) Canting angle dependence of the AHC σ_{AHC} in the CaMnBi$_2$. (c),(d) Band structures in the $k_z = 0$ plane without and with SOC, where the red line is a nodal line protected by the glide plane symmetry and SOC can break the nodal line into opened gaps. The momentum is measured in units of $2\pi/a$.

include the outermost s and d orbitals for Ca, d orbitals for element Mn, and p orbitals for element Bi, which guarantees the full band overlap from *ab initio* and Wannier functions.

B. Symmetry analysis

The crystal structure of AMnBi$_2$ (A = Ca and Yb) with a nonsymmorphic space group $G = P4/nmm$ (No. 129) is shown in Fig. 2(a), where the MnBi$_1$ layers possess an anti-PbO-type atom arrangement and there is a square lattice sheet of Bi$_2$ atoms. Mn and Bi$_2$ atoms occupy the Wyckoff positions $2a$ $\{(0, 0, 0), (1/2, 1/2, 0)\}$ and $2b$ $\{(0, 0, 1/2), (1/2, 1/2, 1/2)\}$, respectively, which have the same corresponding site symmetry group D_{2d}, whereas A and Bi$_1$ atoms occupy the same Wyckoff positions $2c$ $\{(1/2, 0, z), (0, 1/2, -z)\}$ with the corresponding site symmetry group C_{4v}. In the nonsymmorphic space group $G = P4/nmm$, the quotient group G/L is specified by 16 symmetry operations, where L is the translation group with respect to the unit cell. The nonsymmorphic symmetry operations are $\tilde{C}_{2,x} = \{C_{2,x}|1/2, 1/2, 0\}$, $\tilde{C}_{2,y} = \{C_{2,y}|1/2, 1/2, 0\}$ and $\tilde{M}_{xy} = \{M_{xy}|1/2, 1/2, 0\}$ with respect to the original point at the Mn site.

Since the AMnBi$_2$ has AFM order at the Mn atoms with spins along the z axis, we present the following analysis of magnetic space groups and point groups. Choosing the Mn site as the origin, the 16 symmetry operations can be specified equivalently as $D_{2d} \oplus \{I|1/2, 1/2, 0\}D_{2d}$, where I is a space

inversion and the generators of D_{2d} are $C_{2,z}$, $C_{2,xy}$, and M_{xz}. First, owing to the spin at the Mn atoms along the z axis, $C_{2,z}$ cannot alter the direction of spin, while $C_{2,xy}$ and M_{xz} flip spin, indicating that $C_{2,xy}$ and M_{xz} are broken by the AFM order at the Mn atoms. Combined with time reversal symmetry T, we obtain the magnetic point group $\bar{4}2'm'$ corresponding to the point group D_{2d}, whose generators are $C_{2,z}$, $TC_{2,xy}$, and TM_{xz}. Secondly, since the crystal symmetries in the $\tilde{I}D_{2d}$ with $\tilde{I} = \{I|1/2, 1/2, 0\}$ exchange the Mn sublattice and inversion symmetry I cannot flip spin, $C_{2,xy}$ and M_{xz} are maintained while $C_{2,z}$ is broken. This suggests that the magnetic generators corresponding to $\tilde{I}D_{2d}$ are $T\tilde{I}$, $T\tilde{I}C_{2,z}$, $\tilde{I}C_{2,xy}$, and $\tilde{I}M_{xz}$. Finally, based on the above analysis, we find that the magnetic space group of AMnBi$_2$ with AFM order along the z axis is $P4'/n'm'm$ with the magnetic point group $4'/m'm'm$. Due to $T\tilde{I}$ symmetry, the integral of the Berry curvatures on the BZ is forced to zero.

The existence of spin canting in AMnBi$_2$ leads to an in-plane ferromagnetic order, and the magnitude of the canting angle can be experimentally adjusted by doping or temperature [31,32], where they take into account canting angle 10° to explain experimental results. We consider the same canting direction $(1,1,0)$ as in papers in [31,32], which can break the $T\tilde{I}$ symmetry, indicating that AHE can exist. Then, the corresponding magnetic space group becomes $m'm2'$, where the symmetries are $TC_{2,\bar{x}y}$, M_{11}, TM_{xy}, and E, which can host a nonzero AHE.

The AHC tensor can be written as

$$\sigma_{\alpha\beta} = -\sum_n \frac{e^2}{\hbar} \int_{BZ} \frac{d\mathbf{k}}{(2\pi)^3} f_n(\mathbf{k}) \boldsymbol{\Omega}_{n,\alpha\beta}(\mathbf{k}),$$
$$\boldsymbol{\Omega}_{n,\alpha\beta}(\mathbf{k}) = -2 \, \text{Im} \langle \nabla_\alpha u_n(\mathbf{k}) | \nabla_\beta u_n(\mathbf{k}) \rangle, \quad (1)$$

where $\alpha, \beta = x, y, z$ and n is the band index. $f_n(\mathbf{k})$ is the Fermi-Dirac distribution, $|u_n(\mathbf{k})\rangle$ is the eigenvalue of the Hamiltonian, and $\boldsymbol{\Omega}_{n,\alpha\beta}(\mathbf{k})$ is the Berry curvature. Under crystal symmetry g, the relationship of the Berry curvature $\boldsymbol{\Omega}_{n,\alpha\beta}(\mathbf{k})$ between $\mathbf{k}$ and $g\mathbf{k}$ is given by

$$\boldsymbol{\Omega}_{n,\alpha\beta}(g\mathbf{k}) = -2 \, \text{Im} \left\langle \frac{\partial u_n(g\mathbf{k})}{\partial k_\alpha} \middle| \frac{\partial u_n(g\mathbf{k})}{\partial k_\beta} \right\rangle$$
$$= -2 \sum_{\alpha'\beta'} \text{Im} \left\langle \frac{\partial (g\mathbf{k})_{\alpha'}}{\partial \mathbf{k}_\alpha} \frac{\partial u_n(g\mathbf{k})}{\partial (g\mathbf{k})_{\alpha'}} \middle| \frac{\partial (g\mathbf{k})_{\beta'}}{\partial \mathbf{k}_\beta} \frac{\partial u_n(g\mathbf{k})}{\partial (g\mathbf{k})_{\beta'}} \right\rangle$$
$$= \sum_{\alpha'\beta'} \frac{\partial (g\mathbf{k})_{\alpha'}}{\partial \mathbf{k}_\alpha} \frac{\partial (g\mathbf{k})_{\beta'}}{\partial \mathbf{k}_\beta} \boldsymbol{\Omega}_{n,\alpha'\beta'}(\mathbf{k}),$$
$$\boldsymbol{\Omega}_{n,\alpha'\beta'}(\mathbf{k}) = -2 \, \text{Im} \left\langle \frac{\partial u_n(\mathbf{k})}{\partial \mathbf{k}_{\alpha'}} \middle| \frac{\partial u_n(\mathbf{k})}{\partial \mathbf{k}_{\beta'}} \right\rangle. \quad (2)$$

Here, $\frac{\partial (g\mathbf{k})_{\alpha'}}{\partial \mathbf{k}_\alpha} \frac{\partial (g\mathbf{k})_{\beta'}}{\partial \mathbf{k}_\beta}$ is a constant because $g\mathbf{k}$ is a linear function of $\mathbf{k}$. Hence $\frac{\partial (g\mathbf{k})_{\alpha'}}{\partial \mathbf{k}_\alpha} \frac{\partial (g\mathbf{k})_{\beta'}}{\partial \mathbf{k}_\beta}$ is unchanged when we make a substitution $g\mathbf{k} \to \mathbf{k}$. It is clear that the AHC is invariant under the inversion symmetry I, namely $\boldsymbol{\Omega}_{n,\alpha\beta}^\gamma(\mathbf{k}) = \boldsymbol{\Omega}_{n,\alpha\beta}^\gamma(I\mathbf{k})$. Then, we consider the constraint of the magnetic space group $m'm2'$ on the AHC, where considering the mirror symmetry $M_{11} : (\mathbf{k}_x, \mathbf{k}_y, \mathbf{k}_z) \to (-\mathbf{k}_y, -\mathbf{k}_x, \mathbf{k}_z)$ is sufficient. Under the mirror symmetry M_{11}, the transformation of the Berry

curvature $\boldsymbol{\Omega}_{n,\alpha\beta}^\gamma(\mathbf{k})$ can be given by

$$\Omega_{xy}^z(\mathbf{k}) = -\Omega_{xy}^z(M_{11}\mathbf{k}), \quad \Omega_{xz}^y(\mathbf{k}) = -\Omega_{yz}^x(M_{11}\mathbf{k}). \quad (3)$$

Hence, under the constraint of the magnetic space group $m'm2'$, the shape of the AHC tensors is

$$\begin{pmatrix} 0 & 0 & \sigma_{xz} \\ 0 & 0 & -\sigma_{xz} \\ -\sigma_{xz} & \sigma_{xz} & 0 \end{pmatrix}. \quad (4)$$

III. *Ab initio* ANALYSIS OF ANOMALOUS TRANSPORTS

Figures 2(c) and 2(d) show the band structures without and with SOC in the $k_z = 0$ plane, where half of the BZ ($-0.5 < k_x < 0.5$ and $0 < k_y < 0.5$) is shown for the convenience of locating the nodal line. There is a band inversion from the intercalated Bi$_2$ $p_{x/y}$ orbitals, which leads to quasi-two-dimensional band crossing. When the SOC is ignored, the crossing bands can be referred to as K and $K + Q$ bands. Similar to the symmetry analysis of iron superconductors [38], the K and $K + Q$ bands are the different eigenvalues of the glide plane symmetry [30], indicating that the nodal ring from Bi$_2$ $p_{x/y}$ band crossing is robust, as shown in Fig. 2(c). When the on-site SOC is included, the spin-flip term $\langle p_x, \sigma | H_{\text{soc}} | p_y, \bar{\sigma} \rangle$ with the spin index σ can be nonzero [30]. Hence the crossing bands can hybridize each other and the nodal line can be gapped, as shown in Fig. 2(d). Next, we will calculate AHC and consider how the nodal line contributes to AHC.

We calculated the AHC tensor of CaMnBi$_2$ with the Fermi level lying at the charge neutral points. Figure 2(b) shows the canting angle dependence of the AHC σ_{AHC} with spin canting along the $(1,1,0)$ direction, where $\sigma_{\text{AHC}} = \sqrt{\sigma_{xz}^2 + \sigma_{yz}^2} = \sqrt{2}\sigma_{xz}$ owing to $\sigma_{yz} = -\sigma_{xz}$. At a canting angle of 8°, the AHC σ_{AHC} has a small value of 159.50 Ω^{-1}cm^{-1}, whereas it has a large value of 721.90 Ω^{-1}cm^{-1} at a canting angle of 20°. As the canting angle increases from 8° to 20°, the AHC σ_{AHC} continues to grow and is not saturated even if the canting angle reaches 20°. In addition, between 12° and 14°, the rate of increase of the AHC is larger. To explain the variation of the AHC with the canting angle, we consider three (8°, 13°, and 18°) canting angles as examples to calculate band structures and local momentum distribution of the Berry curvature in the BZ with spin canted C-type AFM states, where the magnitude of the magnetic moments in the xy plane (z direction) are 0.53μ_B (3.81μ_B), 0.99μ_B (3.74μ_B), and 1.31μ_B (3.63μ_B), respectively.

First, Fig. 3(a) shows band structures at a canting angle of 8°. Near the Fermi level, the valence and conduction bands are mainly attributed to the p orbitals of the intercalated Bi$_2$ atoms, similar to band structures without a canting angle [32]. The bands are split into spin up and spin down owing to the ferromagnetic order in the xy plane. The small hole pockets around the Γ point are dominated by the intercalated Bi$_2$-p_z (blue) orbital, which is remarkably split because of hybridizing with the Mn d orbitals. The electronic pockets from the nodal line originate mainly from the intercalated Bi$_2$-$p_{x/y}$ (green) orbitals, which are less sensitive to the ferromagnetic order in the xy plane and are hardly split. Figure 3(d) shows the local momentum distribution of the Berry curvature in
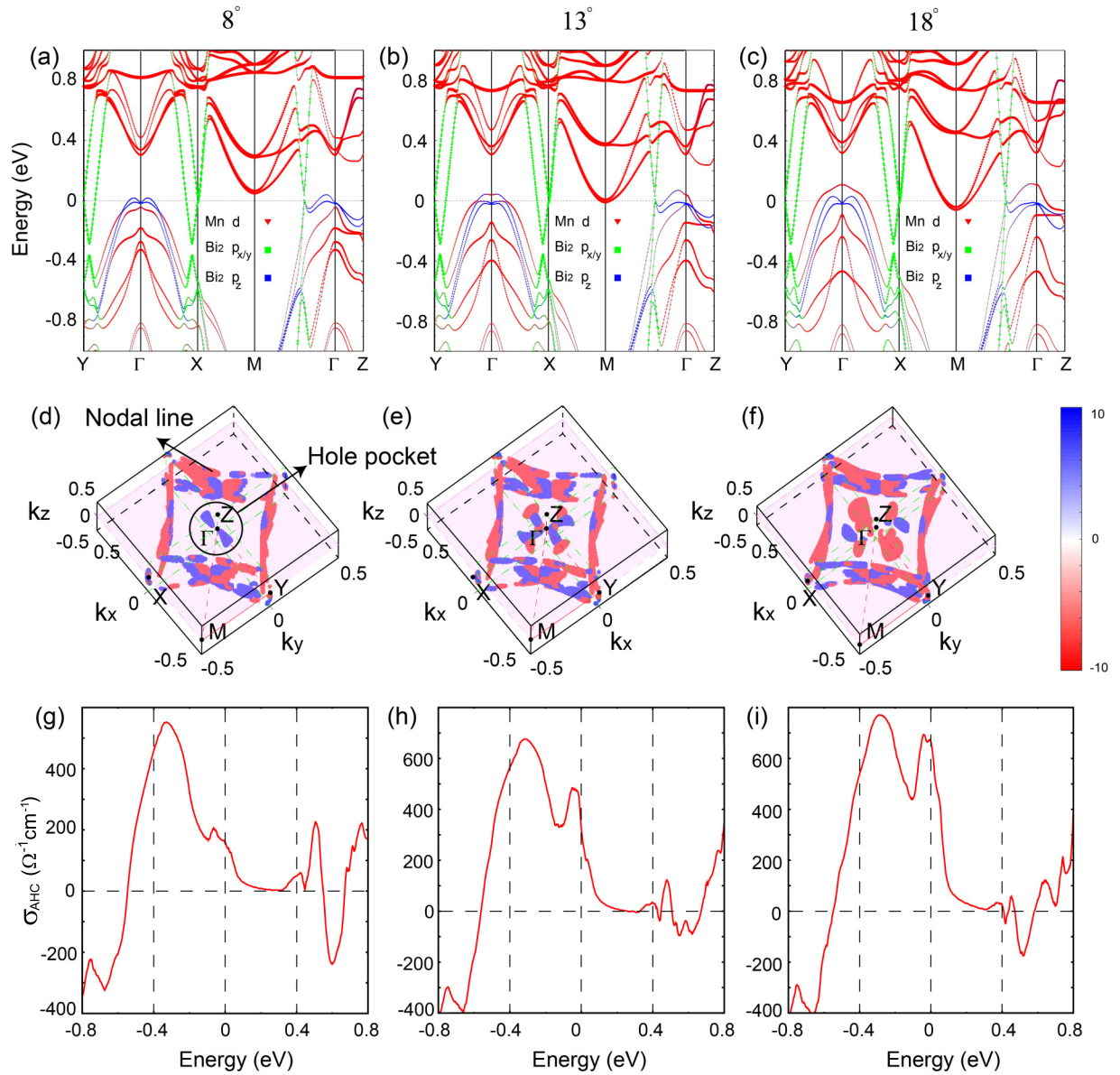
FIG. 3. (a)–(c) Band structures with spin canted C-type AFM states at canting angles of 8°, 13°, and 18°, respectively. The orbital characters of the bands are represented by different colors. Panels (d)–(f) show the local momentum distribution of the Berry curvature in the BZ σ_{total} at canting angles of 8°, 13°, and 18°, respectively. (g)–(i) Energy-dependent AHC σ_{AHC} at canting angles of 8°, 13°, and 18°, respectively.

the BZ at 8° canting angle. Around the Γ point, the Berry curvatures are mainly contributed by hole pockets with a small volume and positive. The Berry curvatures near the nodal line dominated by the electronic pockets are negative and large volumes. Since the value of AHC σ_{AHC} is 159.50 Ω^{-1}cm^{-1}, the integral of them gives a negative net Berry curvature, namely, a positive AHC. The nodal line has dispersion in the BZ, which can result in electronic pockets at the Fermi level. Hence the nodal line is mainly responsible for nonzero AHC.

Second, when the canting angle is increased to 13°, the splits of the band structures become larger as the magnitude of the ferromagnetic order in the xy plane increases. Then, the electronic pockets from the nodal line have more splits, which may strengthen AHC. The Mn d-orbital bands can also attribute a hole pocket near the Γ point, which can result in a positive Berry curvature, as shown in Figs. 3(b) and

3(e). Hence the AHC corresponding to the canting angle of 13° exceeds that of 8°, as shown in Fig. 2(b). Finally, when the canting angle is further increased to 18°, a large hole pocket near the Γ point is completely contributed by the Mn-d orbitals owing to the large band splits induced by strong ferromagnetism. The large hole pocket can cause a large and negative Berry curvature, indicating that the AHC at a canting angle of 18° increases, as shown in Figs. 3(c) and 3(f).

Here, we summarize the analysis above. We find that the ferromagnetism in the xy plane increases with the canting angle, which can cause greater splits in the band structures. Then, the hole pocket contributed by the Mn d orbitals will become larger, and can cause large and negative Berry curvature. Moreover, the electronic pockets from the nodal line mainly contribute to the AHC, indicating that it is responsible for nonzero AHC. As the ferromagnetism increases, the
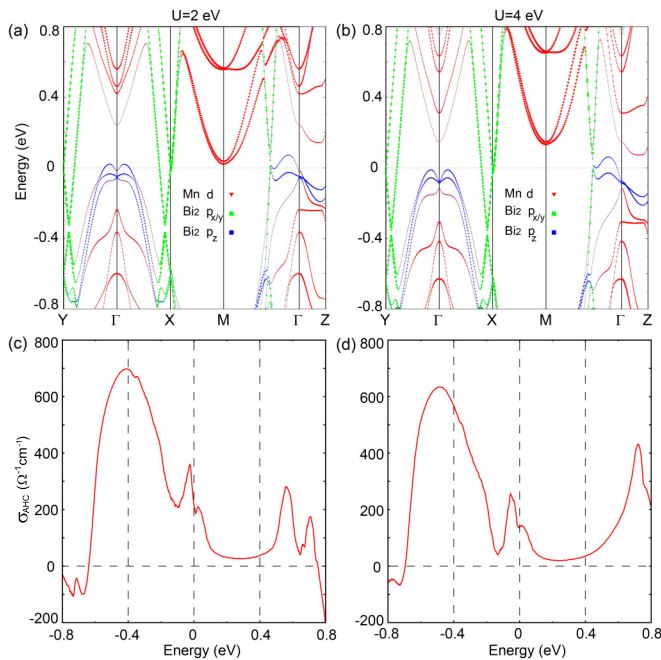
FIG. 4. Band structures and the corresponding energy-dependent AHC tensor σ_{AHC} when the effective on-site Coulomb U are (a),(c) 2 eV and (b),(d) 4 eV for the Mn d orbitals at a canting angle of $18°$ in the GGA+U calculation.

electronic pockets split further, which can strengthen the AHC. Therefore, in the range of canting angles we consider, the AHC continues to grow as the canting angle increases.

To further explore the effect of hole and electron doping on the AHC σ_{AHC}, Figs. 3(d)–3(f) show the energy-dependent AHC σ_{AHC} calculated from the Berry curvature at canting angles of $8°$, $13°$, and $18°$. When the Fermi level is at the charge neutral points, the AHC σ_{AHC} are 110, 230, and 470 Ω^{-1}cm^{-1}, respectively, indicating continuous growth of the AHC as the canting angle increases. At canting angles of $13°$ and $18°$, a peak in σ_{AHC} appears around the Fermi level, as shown in Figs. 3(e) and 3(f). In addition, in three cases, near Fermi level doping electrons can reduce AHC, while doping holes strengthen it.

In order to consider the effect of the correlation effect on AHC in the canted C-type AFM order, Fig. 4 shows band structures and AHC when the effective on-site Coulomb U are 2 eV and 4 eV for the Mn d orbitals at a canting angle of $18°$ in the GGA+U calculation. The gap between the Mn d

orbitals (red) increases as U increases, while the band structures attributed by intercalated Bi$_2$ p orbitals (green and blue) remain unchanged, as shown in Figs. 4(a) and 4(b). Compared to the band structures without U, the d-orbital bands with U stay away from the Fermi level, and the bands at the Fermi level are mainly attributed to the Bi$_2$ p orbitals. Figures 4(c) and 4(d) show the energy-dependent AHC tensor σ_{AHC} when U are 2 eV and 4 eV for the Mn d orbitals at a canting angle of $18°$, and the AHC tensors σ_{AHC} with U are small compared to those without U, indicating that the correlation effect can suppress AHC.

Since spin canting exists in YbMnBi$_2$, we calculate the AHC tensors and band structures of YbMnBi$_2$ at different canting angles. Similar to CaMnBi$_2$, the ferromagnetism in the xy plane increases with the canting angle, and the hole pocket at the Γ point contributed by the Mn d orbitals becomes larger, resulting in large and negative Berry curvature. Therefore, the AHC σ_{AHC} in the YbMnBi$_2$ also increases as the canting angle increases. The energy-dependent AHC σ_{AHC} is also calculated at different canting angles, and doping electrons is found to suppress AHC while doping holes strengthens it.

IV. CONCLUSION

In summary, the AHE in the layered ternary material AMnBi$_2$ (A = Ca and Yb) with spin canted C-type antiferromagnetic order can be studied based on first-principles calculations and symmetry analysis. Considering the canting along the (1,1,0) direction, the magnetic space group is $m'm2'$, and only $\sigma_{xz/yz}$ in the AHC tensors is nonzero because of mirror symmetry. We find that the AHC σ_{AHC} grows continuously with the canting angle increasing, and doping electrons can reduce AHC while doping holes strengthens it. The correlation effect from the Mn d orbitals is considered, and it can suppress AHC. This work provides an effective design strategy and corresponding materials for obtaining a strong AHE.

[1] N. Nagaosa, J. Sinova, S. Onoda, A. H. MacDonald, and N. P. Ong, Rev. Mod. Phys. **82**, 1539 (2010).

[2] Z. Fang, N. Nagaosa, K. S. Takahashi, A. Asamitsu, R. Mathieu, T. Ogasawara, H. Yamada, M. Kawasaki, Y. Tokura, and K. Terakura, Science **302**, 92 (2003).

[3] F. D. M. Haldane, Phys. Rev. Lett. **93**, 206602 (2004).

[4] D. Xiao, M. C. Chang, and Q. Niu, Berry phase effects on electronic properties, Rev. Mod. Phys. **82**, 1959 (2010).

[5] E. Liu, Y. Sun, N. Kumar, L. Muechler, A. Sun, L. Jiao, S.-Y. Yang, D. Liu, A. Liang, Q. Xu, J. Kroder, V. Su, H. Borrmann, C. Shekhar, Z. Wang, C. Xi, W. Wang, W. Schnelle, S. Wirth, Y. Chen, S. T. B. Goennenwein, and C. Felser, Nat. Phys. **14**, 1125 (2018).

[6] Q. Wang, Y. Xu, R. Lou, Z. Liu, M. Li, Y. Huang, D. Shen, H. Weng, S. Wang, and H. Lei, Nat. Commun. **9**, 3681 (2018).

[7] Q. Xu, E. Liu, W. Shi, L. Muechler, J. Gayles, C. Felser, and Y. Sun, Phys. Rev. B **97**, 235416 (2018).

[8] C. Tan, J. Lee, S.-G. Jung, T. Park, S. Albarakati, J. Partridge, M. R. Field, D. G. McCulloch, L. Wang, and C. Lee, Nat. Commun. **9**, 1554 (2018).

[9] K. Kim, J. Seo, E. Lee, K.-T. Ko, B. S. Kim, B. G. Jang, J. M. Ok, J. Lee, Y. J. Jo, W. Kang, J. H. Shim, C. Kim, H. W. Yeom, B. I. Min, B.-J. Yang, and J. S. Kim, Nat. Mater. **17**, 794 (2018).

[10] S. N. Guin, K. Manna, J. Noky, S. J. Watzman, C. Fu, N. Kumar, W. Schnelle, C. Shekhar, Y. Sun, J. Gooth, and C. Felser, NPG Asia Mater. **11**, 16 (2019).

[11] P. Li, J. Koo, W. Ning, J. Li, L. Miao, L. Min, Y. Zhu, Y. Wang, N. Alem, C.-X. Liu, Z. Mao, and B. Yan, Nat. Commun. **11**, 3476 (2020).

[12] J. Kubler and C. Felser, Europhys. Lett. **114**, 47005 (2016).

[13] J. Noky, Q. Xu, C. Felser, and Y. Sun, Phys. Rev. B **99**, 165117 (2019).

[14] K. Manna, Y. Sun, L. Muechler, J. Kubler, and C. Felser, Nat. Rev. Mater. **3**, 244 (2018).

[15] K. Manna, L. Muechler, T.-H. Kao, R. Stinshoff, Y. Zhang, J. Gooth, N. Kumar, G. Kreiner, K. Koepernik, R. Car, J. Kubler, G. H. Fecher, C. Shekhar, Y. Sun, and C. Felser, Phys. Rev. X **8**, 041045 (2018).

[16] R. Shindou and N. Nagaosa, Phys. Rev. Lett. **87**, 116801 (2001).

[17] H. Chen, Q. Niu, and A. H. MacDonald, Phys. Rev. Lett. **112**, 017205 (2014).

[18] J. Kubler and C. Felser, Europhys. Lett. **108**, 67001 (2014).

[19] S. Nakatsuji, N. Kiyohara, and T. Higo, Nature (London) **527**, 212 (2015).

[20] A. K. Nayak, J. E. Fischer, Y. Sun, B. Yan, J. Karel, A. C. Komarek, C. Shekhar, N. Kumar, W. Schnelle, J. Kubler, C. Felser, and S. S. P. Parkin, Sci. Adv. **2**, e1501870 (2016).

[21] Y. Zhang, Y. Sun, H. Yang, J. zelezny, S. P. P. Parkin, C. Felser, and B. Yan, Phys. Rev. B **95**, 075128 (2017).

[22] R. D. dos Reis, M. Ghorbani Zavareh, M. O. Ajeesh, L. O. Kutelak, A. S. Sukhanov, S. Singh, J. Noky, Y. Sun, J. E. Fischer, K. Manna, C. Felser, and M. Nicklas, Phys. Rev. Materials **4**, 051401(R) (2020).

[23] W. Shi, L. Muechler, K. Manna, Y. Zhang, K. Koepernik, R. Car, J. van den Brink, C. Felser, and Y. Sun, Phys. Rev. B **97**, 060406(R) (2018).

[24] Z. Feng, X. Zhou, L. mejkal, L. Wu, Z. Zhu, H. Guo, R. Gonzalez-Hernandez, X. Wang, H. Yan, P. Qin, X. Zhang, H. Wu, H. Chen, C. Jiang, M. Coey, J. Sinova, T. Jungwirth, and Z. Liu, arXiv:2002.08712.

[25] X. Li, A. H. MacDonald, and H. Chen, arXiv:1902.10650.

[26] J. B. He, D. M. Wang, and G. F. Chen, Appl. Phys. Lett. **100**, 112405 (2012).

[27] A. Wang, D. Graf, L. Wu, K. Wang, E. Bozin, Y. Zhu, and C. Petrovic, Phys. Rev. B **94**, 125118 (2016).

[28] A. Zhang, C. Liu, C. Yi, G. Zhao, T. L. Xia, J. Ji, Y. Shi, R. Yu, X. Wang, C. Chen, and Q. Zhang, Nat. Commun. **7**, 13833 (2016).

[29] Z. Qiu, C. Le, Y. Dai, B. Xu, J. B. He, R. Yang, G. Chen, J. Hu, and X. Qiu, Phys. Rev. B **98**, 115151 (2018).

[30] Z. Qiu, C. Le, Z. Liao, B. Xu, R. Yang, J. Hu, Y. Dai, and X. Qiu, Phys. Rev. B **100**, 125136 (2019).

[31] S. Borisenko, D. Evtushinsky, Q. Gibson, A. Yaresko, K. Koepernik, T. Kim, M. Ali, J. van den Brink, M. Hoesch, A. Fedorov, E. Haubold, Y. Kushnirenko, I. Soldatov, R. Schafer, and R. J. Cava, Nat. Commun. **10**, 3424 (2019).

[32] R. Yang, M. Corasaniti, C. C. Le, Z. Y. Liao, A. F. Wang, Q. Du, C. Petrovic, X. G. Qiu, J. P. Hu, and L. Degiorgi, Phys. Rev. Lett. **124**, 137201 (2020).

[33] G. Kresse and J. Hafner, Phys. Rev. B **47**, 558 (1993).

[34] G. Kresse and J. Furthmuller, Comput. Mater. Sci. **6**, 15 (1996).

[35] G. Kresse and J. Furthmuller, Phys. Rev. B **54**, 11169 (1996).

[36] H. J. Monkhorst and J. Pack, Phys. Rev. B **13**, 5188 (1976).

[37] J. R. Yates, X. Wang, D. Vanderbilt, and I. Souza, Phys. Rev. B **75**, 195121 (2007).

[38] X. Wu, S. Qin, Y. Liang, H. Fan, and J. Hu, Phys. Rev. B **93**, 115129 (2016).